IEEE Access
Multidisciplinary ⋮ Rapid Review ⋮ Open Access Journal

Received 21 March 2023, accepted 8 April 2023, date of publication 13 April 2023, date of current version 19 April 2023.

*Digital Object Identifier 10.1109/ACCESS.2023.3266989*

RESEARCH ARTICLE

# Projection Matrix Based Iterative Reconstruction Algorithm for Robotic CT

**XUAN ZHOU[1,2], QIONG XU[1,3], AND CUNFENG WEI[1,2,3]**

[1]Beijing Engineering Research Center of Radiographic Techniques and Equipment, Institute of High Energy Physics, Chinese Academy of Sciences, Beijing 100049, China
[2]School of Nuclear Science and Technology, University of Chinese Academy of Sciences, Beijing 100049, China
[3]Jinan Laboratory of Applied Nuclear Science, Jinan 250131, China

Corresponding author: Cunfeng Wei (weicf@ihep.ac.cn)

This work was supported in part by the National Natural Science Foundation of China under Grant 12175267 and Grant 11975250.

**ABSTRACT** Robotic computed tomography (CT) consists of two separate manipulators which carry the source and detector, respectively. Various errors occur in motion due to lack of rigid connection, which may change scanning trajectory of this system. Some methods aimed at recovering geometry relation have occurred. However, these methods are relied on circular scanning trajectory. Projection matrix is the matrix form of geometry definition, which contains geometric parameters in the matrix and transforms geometry calculation into homogeneous matrix calculation. It is suitable for robotic CT because of its irrelevance between angles. Besides, iteration reconstruction algorithm makes no assumptions on scanning trajectories, which is suitable for arbitrary scanning trajectories. Hence, this study combines iteration reconstruction algorithm with the concept of projection matrix to fill the gap. In this study, we established a transformation between projection matrix and ray function, and construct corresponding projection model. Projection matrix based iterative reconstruction algorithm was then developed and validated by simulation and experiment. Uncooperative rotation of manipulators, jitter in motion and non-circular motion trajectories were simulated. FDK, projection matrix-based FDK and projection matrix-based iterative method were compared. Real experiments were also conducted. The results showed projection matrix based iterative reconstruction could lead to better image quality against motion error. In summary, this study provided a high-precision reconstruction approach for robotic CT.

**INDEX TERMS** Robotic CT, calibration phantom, projection matrix.

## I. INTRODUCTION

Robotic computed tomography (CT) is a novel CT structure which uses two manipulators to carry the source and detector, respectively. It differs from conventional CT structures like gantry CT and C-arm with no mechanical link between two manipulators. As a result, it can adjust geometry parameters before and during scanning to adapt to object size. Projection data are acquired through rotation of manipulators around object. However, motion error may occur during this rotation because of limited mechanical accuracy. Direct reconstruction without calibration will bring in artifacts in images.

Calibration methods of robotic CT are derived from conventional CT like cone-beam CT. Some of these calibration techniques rely on specific scanning trajectory [1], [2], [3], or make an assumption of structure information [4], [5], [6]. Such prerequisites are not satisfied in robotic CT because of its special structure hence these methods are not appropriate for this new system. There are also methods intended to offer geometry information of single angles [7], [8], [9]. Majority of these methods are based on well-designed calibration phantoms. The helical configuration phantom [10] is the most popular design among these phantoms, because it can avoid overlap of markers in almost all angles, which benefits extraction of markers. After acquiring projections of the phantom, geometry calibration can be performed through nonlinear optimization [11], [12], or linear optimization followed by

The associate editor coordinating the review of this manuscript and approving it for publication was Yi Zhang.

parameters decomposition [13]. The former created projection relation using specified geometric parameters, combined it with coordinates of marker points and their corresponding projection points to create nonlinear equations, then used optimization concept to obtain the solution of equations. The latter first expresses projection relation as homogeneous coordinates, calculates projection relation in the homogeneous coordinate system by creating linear equations, specific geometric parameters are then gained by matrix decomposition. It does not directly associate geometric parameters with the coordinates of markers. Accuracy of geometry parameters for both methods rely on the precision of calibration phantom.

However, various kinds of mistake may be introduced during calculation, which increased the requirements for phantom's precision. As image resolution has been gradually improving, phantom's precision is usually insufficient, which may result in error in geometry parameters [12]. Researchers have done some work on this problem. Some aimed at exploring phantom-free calibration method [14], [15], [16]. Li et.al [17] proposed a locally linear embedding-based motion correction method which alternately optimized system geometry and reconstruction images without accurate phantom, this method got rid of the dependence of calibration phantom and had obtained excellent performance in practical experiments. Some researchers focused on improving the accuracy of phantom. Xu et.al [18] set phantom error index integrated with image quality index as object function, and simultaneously improved phantom precision and image quality through optimization. Duan et.al [19] gathered multiple projections through separately moving source position. Coordinates of markers under these projections were then used in an optimization of phantom markers. But these phantom calibration methods also have limitations, error may be introduced by additional calibration process, which limit final phantom precision after these phantom calibration methods. Additionally, some are too complex to be applied in practice. Meanwhile, some researchers noticed the intermediate product called projection matrix during geometry calibration can be directly used in reconstruction, which may reduce calculation error to some extent. So they introduced FDK based on projection matrix [20] by combining projection matrix with back-projection process. However, the FDK model is the foundation of this reconstruction approach, which is based on circular scanning trajectory and may cause abnormality in gray value when facing mechanical motion error.

In this paper, we proposed a projection matrix-based iterative reconstruction method to fulfill this gap. In both forward and backward projection process, we used projection matrix to define projection geometry. A line-driven forward projection model and a point-driven backward projection model were established. The method was made up of these two models as well as regularization term structure.

This paper is organized as follows: Section II explains the notion of traditional projection geometry and projection matrix, followed by the fundamentals of forward and backward projection model. The conditions of simulation experiment and actual data will be covered in section III. Results are shown in section IV. Section V is discussion and conclusion.

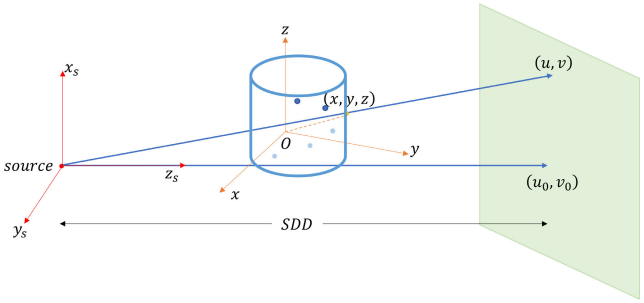


**FIGURE 1.** Typical projection geometry.

## II. METHODS AND MATERIALS

### A. PROJECTION MATRIX

A typical projection geometry is shown in Fig. 1, *source* denotes the source of ray, $O - xyz$ represents the phantom coordinate system, $source - xyz$ represents the coordinate system of source, $(u_0, v_0)$ represents the projection point of source vertically to the detector, and *SDD* is the distance between source and $(u_0, v_0)$ point. An integral point in phantom coordinate system is expressed as $(x, y, z)$, and its corresponding projection point is $(u, v)$. The projection matrix $P$ gives a homogenous description of projection connection from phantom coordinate system to the detector. The matrix form is as follows:

$$[uw, vw, w]^T = P \cdot [x, y, z, 1]^T \tag{1}$$

where $w$ is a distance weighting factor, and $P$ is a $3 \times 4$ projection matrix, which is:

$$P = \begin{bmatrix} P_{11} & P_{12} & P_{13} & P_{14} \\ P_{21} & P_{22} & P_{23} & P_{24} \\ P_{31} & P_{32} & P_{33} & P_{34} \end{bmatrix} \tag{2}$$

The projection matrix is composed of a $3 \times 3$ intrinsic matrix, a $3 \times 3$ rotation matrix, and a $3 \times 1$ translation vector, named $K$, $R$ and $t$, respectively.

$$P = K \cdot [R \quad t] \tag{3}$$

where $R$ and $t$ represent rotation and translation transformation from object coordinate system into source coordinate system. And $K$ stands for the projection process in the source coordinate system. According to Eq.1, linear equations can be established after gaining coordinates of marker points and its corresponding projection points. By eliminating weighting factor $w$, two separate linear equations can be established using coordinates of one pair of marker point.

$$\begin{aligned} P_{11}x + P_{12}y + P_{13}z + P_{14} &= u\,(P_{31}x + P_{32}y + P_{33}z + P_{34}) \\ P_{21}x + P_{22}y + P_{23}z + P_{24} &= v\,(P_{31}x + P_{32}y + P_{33}z + P_{34}) \end{aligned} \tag{4}$$

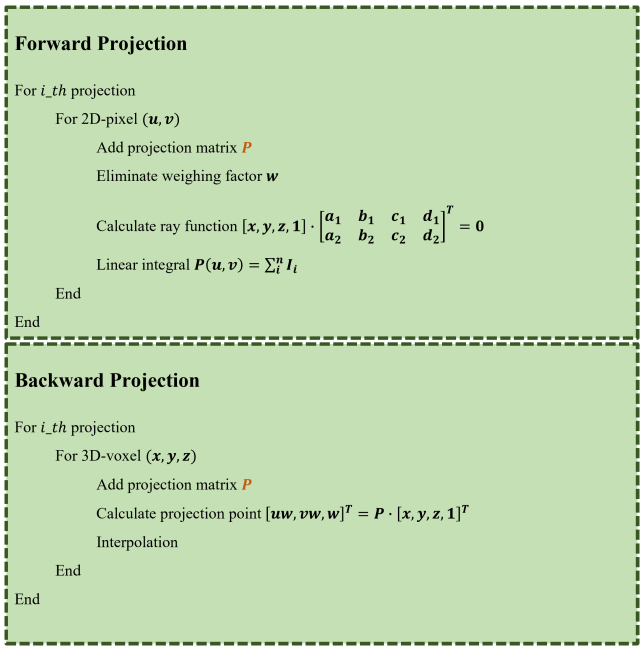


**FIGURE 2.** Structure of FP and BP models.

where variables are twelve elements of matrix $P$ in Eq.2. When given coordinates of multiple pairs of markers, an overdetermined system of linear equation was established.

$$AP_{vector} = 0$$
$$P_{vector} = [P_{11}P_{12}\cdots P_{21}P_{22}\cdots P_{33}P_{34}]^T \quad (5)$$

where $A$ contained the coefficient in Eq.4.

Problem-solving of Eq.5 is a traditional linear least squares problem, which can be solved through singular value decomposition (SVD). Detailed solution was described in [13].

### B. PROJECTION MATRIX BASED FORWARD AND BACKWARD PROJECTION

The coordinates of the marker points and the related projection points of single angles can be used to calculate the projection matrix $P$. The projection relation is equal to the ray equation, and it is known that the projection matrix can express the projection relation under single angles. As a result, during forward projection, the projection matrix can be used to find linear equation of projection ray and this linear equation can be used to calculate projection value. Back-projection value can be gained by calculating the two-dimensional projection point corresponding to a voxel point and applying interpolation, matrix multiplication can be used in the back projection under the homogeneous coordinate system. The process of FP and BP algorithms were shown in Fig.2. Besides, the regularization terms can be incorporated into iterative reconstruction to improve the reconstruction quality. Final image $X^*$ was obtained by:

$$X^* = \arg\min \|AX - P\|_2^2 + R \quad (6)$$

where $R$ is the regularization term, $A$ is the coefficient term of reconstruction, and $X$, $P$ are images and projections, respectively. We used TV minimization for regularization in the reconstructions presented in this paper.

#### 1) FORWARD PROJECTION

The projection matrix $P$ is presented in manner depicted in Eq. 2. By removing the distance weighting factor $w$, we obtain:

$$[x, y, z, 1] \cdot \begin{bmatrix} P_{11} - uP_{31} & P_{21} - vP_{31} \\ P_{12} - uP_{32} & P_{22} - vP_{32} \\ P_{13} - uP_{33} & P_{23} - vP_{33} \\ P_{14} - uP_{34} & P_{24} - vP_{34} \end{bmatrix} = 0 \quad (7)$$

It can be simplified as follows:

$$[x, y, z, 1] \cdot \begin{bmatrix} a_1 & b_1 & c_1 & d_1 \\ a_2 & b_2 & c_2 & d_2 \end{bmatrix}^T = 0 \quad (8)$$

The equation for the line projected to point $(u, v)$ in the modular coordinate system's is Eq. 8. Calculating projection value through the phantom space comes after obtaining the line's equation. The line integral of the ray traversing the voxel space is the projection. It takes a lot of processing power to calculate intersection of grid and the line after laboriously converting coordinate system space into grid space. Therefore, we streamlined the model by consulting earlier research. We drastically reduced the computation by turning the threedimensional space of coordinate system into a multilayer structure and replacing the integral length of the ray through voxel element with an interpolation of intersection point between ray and single-layer center. In the new model, the linear direction vector is determined as follows:

$$l = \begin{bmatrix} i & j & k \\ a_1 & b_1 & c_1 \\ a_2 & b_2 & c_2 \end{bmatrix} \quad (9)$$

where $i, j, k$ represent three space unit vectors. Then voxel space is divided along the $x$, $y$, or $z$ axes depending on the ray vector's direction. After that, a set of two-dimensional layers is created from the voxel space. Take a segmentation in the $x$ direction as an example. The two-dimensional layers' corresponding $x$ coordinate is:

$$x_i = \frac{i-1}{2}, where\ i = 1, 2 \ldots n \quad (10)$$

First, determine the coordinates of the intersection point where the line crosses the single-layer image $(y_i, z_i)$ in order to calculate the projection:

$$\begin{bmatrix} y_i \\ z_i \end{bmatrix} = \begin{bmatrix} \left(\frac{c_1}{c_2}d_2 - d_1 - \left(a_1 - \frac{c_1}{c_2}a_2\right)x\right) / \left(b_1 - \frac{c_1}{c_2}b_2\right) \\ \left(\frac{b_1}{b_2}d_2 - d_1 - \left(a_1 - \frac{b_1}{b_2}a_2\right)x\right) / \left(c_1 - \frac{b_1}{b_2}c_2\right) \end{bmatrix} \quad (11)$$

Then the points $(x_i, y_i, z_i)$ are interpolated:

$$I_i = \left| \begin{bmatrix} up_y - y_i \\ y_i - down_y \end{bmatrix}^T \begin{bmatrix} I(d,d) & I(d,u) \\ I(u,d) & I(u,u) \end{bmatrix} \begin{bmatrix} up_z - z_i \\ z_i - down_z \end{bmatrix} \right| \quad (12)$$

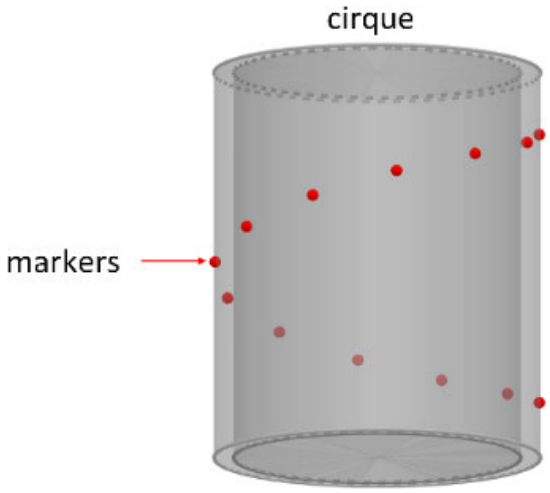


**FIGURE 3.** Schematic diagram of the digital calibration phantom.

where $up_m$ and $down_m$ represent the round up and down of a given variable $m$. $I\,(u(d), u(d))$ stands for the pixel value of corresponding round up or down projection point. The integral value of image interpolation at each layer is the projection value of the final ray:

$$P\,(u, v) = \sum_{i}^{n} I_i \tag{13}$$

#### 2) BACKWARD PROJECTION

When it comes to backward projection, its theory stays consistent with the projection matrix-based FDK algorithm. The voxel points are traversed in the homogeneous coordinate system, and corresponding projection point coordinates are computed point by point using the two-dimensional interpolation within projection images.

## III. EXPERIMENTS CONDITION

In this study, simulation and experiments were conducted to verify the feasibility of proposed iterative method. In simulation, motion error of robotic CT was divided into three cases, which were deviation of two manipulator's rotation, jitter in rotation of manipulator, and non-circular rotation of source, respectively. For comparison, we used FDK, projection matrix based FDK(P-FDK) and projection matrix based SART(P-SART) in reconstruction. For simulation and experiment, we used offline correction technique. A calibration was performed before the scan. The calibration phantom used in simulation was generated according to parameters of real plastic phantom.

A plexiglass hollow cylinder with 13 markers points was generated through digital phantom generator [21], which was shown in Fig.3. No error was added into position of markers.

It was worth mentioning that the repeated positioning accuracy of robotic arm was 50 $\mu m$, which was much smaller than motion error of robot CT. It was assumed to be negligible in experiments. The calibration phantom was placed inside FOV, and projection images of every single view was collected. The circle center of projected circle of markers was gathered through the Hough transform algorithm.

### A. SIMULATION

The simulation experiments were performed on a self-made simulation platform, which was improved from the ASTRA simulation platform [22]. The platform adopted line-driven forward projection and point-driven back-projection models.

In simulation, we used a self-made digital phantom, which came from real data. The geometry was defined according to real situation, with 810 *mm* as source to detector distance (SDD), and 540 *mm* as source to center distance (SOD). Detector size was $536 \times 536$, with pixel size of 0.8 *mm*. Image size was $536 \times 536$ pixels, with unit size of 0.4 *mm*.

We performed one simulation without noise first to analyze algorithm performance under ideal situation. Then we added noise to simulate performance in real situation. Complete flow chart of simulation was shown in Fig. 4.

#### 1) SIMULATION OF UNCOOPERATIVE ROTATION

The motion range used in simulation was generated by referring to actual motion of the manipulator. Two manipulators in real activity may have different rotation speed under different load. Therefore, we assumed that rotation angle of ray source gradually fell behind detector under a continuous scanning mode in simulation. The maximum angle variation was determined at 0.68°. Deviation of in each angle was first evenly split by maximal angel deviation, then a Gaussian random deviation was added into it. The final deviation of rotation angle was displayed in Fig. 5.

#### 2) SIMULATION OF JITTER

This case was introduced in order to simulate mechanical unsteadiness in real situation. In simulation, both source and detector rotated around the center point. We added Gaussian random deviation into three components of position, for both source and detector. The standard deviation of this deviation was 0.5 *mm*. The deviation value of source position in each scanning angle was shown in Fig. 6.

#### 3) SIMULATION OF NON-CIRCLE SCANNING TRAJECTORY

In the simulation experiment, in order to simulate scanning trajectory in real system, only the motion trajectory of the ray source was elliptical while trajectory of detector stays circular. The detector and ray source rotate at same angle. Eccentricity of ellipse trajectory was set at 0.7. Motion trajectories of source and detector was displayed in Fig. 7.

### B. EXPERIMENTS

A turkey leg was scanned in experiment, with 120 *kV* and 100 *mAs*. Geometry parameters were 810 *mm* of SDD, 540 *mm* of SOD. A calibration was performed first with a well-designed phantom. Projections within 200° were collected due to physical limitation of scanning space.

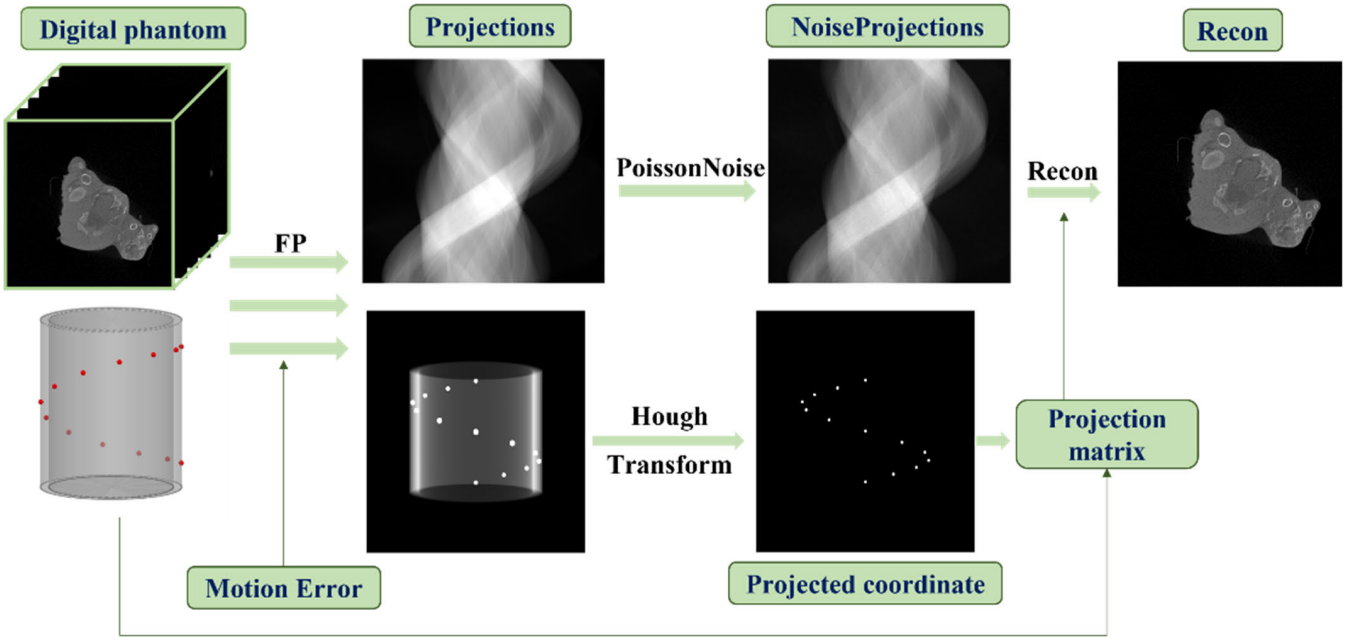


**FIGURE 4.** Flowchart of simulation.

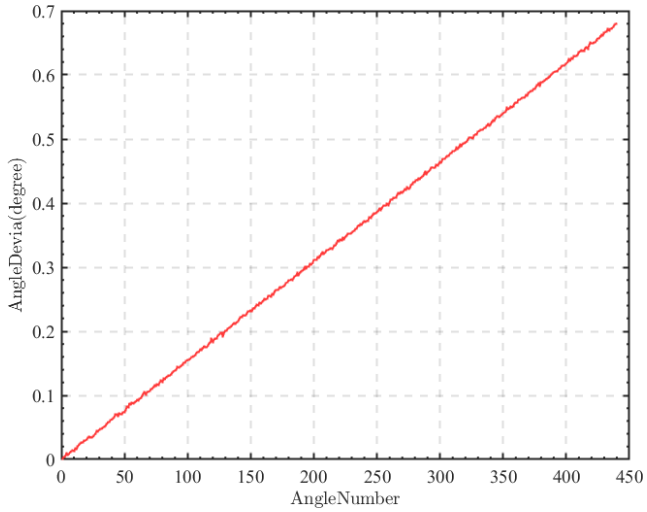


**FIGURE 5.** Deviation of rotation angle between source and detector.

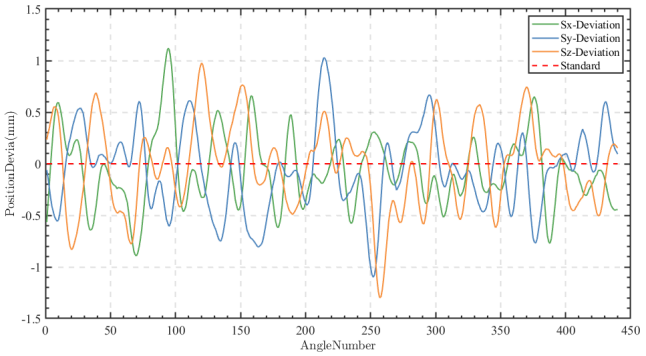


**FIGURE 6.** Deviation of source position in each scanning angle.

#### 1) ROBOTIC CT IN LABORATORY

Fig. 8 depicted robotic CT system in laboratory, which consisted of two robotic arms that held a ray source and detector. The translation stage was placed in the center. During scanning, object was rotated by two robotic arms to capture projected images. The manipulator's positioning accuracy was roughly 0.5 *mm*.

#### 2) CALIBRATION PHANTOM

The special designed phantom was displayed in Fig. 9. It was made of thirteen steel balls placed in a plexiglass ring.

The ball's diameter was 3 *mm*, and the precision of its position was 0.05 *mm*. The plexiglass ring was 76 *mm* in height, and the outer and inner diameter length were 90 *mm* and 77 *mm*, respectively.

#### 3) EVALUATION INDEX

In simulation and experiments, the quality of the reconstructed image was used to evaluate the validity. The peak signal to noise ratio (PSNR) and structure similarity index measure (SSIM) values of reconstructed images were also be considered in the simulation experiment.

## IV. RESULTS

### A. SIMULATION RESULTS

Reconstructed images using FDK, P-FDK, P-SART and P-SART-TV were shown in Fig. 10, among which FDK was conducted under a standard circular geometry. The gray scale range of reconstructed images was [0,0.035]. Case 1-3 represents simulation of uncooperative rotation, jitter and non-circular scanning trajectory.

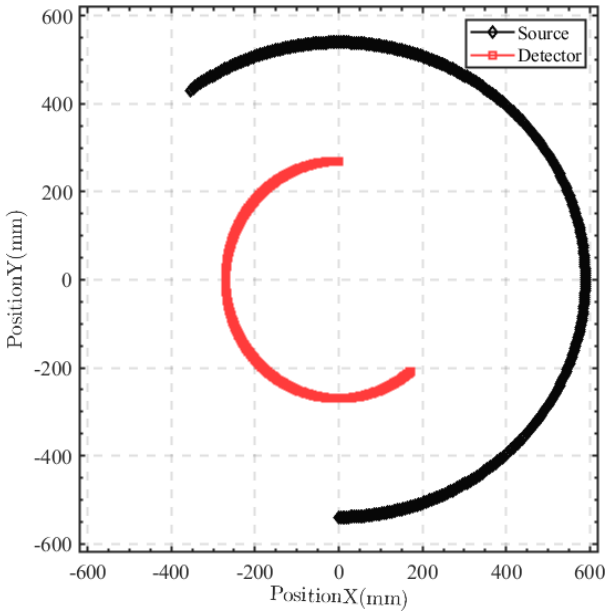


**FIGURE 7.** Elliptic scanning trajectory in simulation.

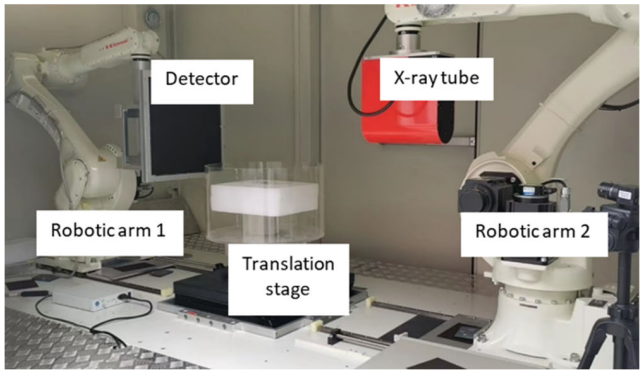


**FIGURE 8.** Robotic CT system in laboratory.

We could see that in all three cases, P-SART and P-SART-TV had similar performance, and the two methods had the best image quality among all algorithms. Besides, in case 1 and case 2, P-FDK algorithm and the two SART methods had similar performance under these motion error. And image evaluation index showed barely the same value of these methods. Meanwhile, three projection matrix-based methods had obvious improvement compared with direct FDK without calibration. While in case 3, although there was no obvious structural misalignment in images, structure similarity index indicated that brightness of images was dramatically different from real images. In case 1 and case 3, motion error during scan brough in obvious structural artifacts in reconstructed images of FDK algorithm. While in case 2, the jitter during rotation of manipulators would also bring in artifacts in images, which was more like interference by noise. In addition, P-SART with the absence of TV achieved slightly better performance than the one with TV regularization, which could be explained by strict constrains on image gradient brought by TV.

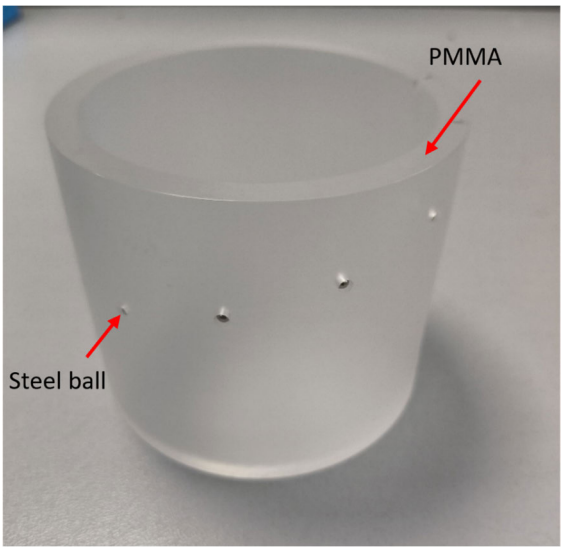


**FIGURE 9.** Calibration phantom in laboratory.

Fig. 11 showed results under Poisson noise interference. The gray scale displayed was also [0,0.035]. We could see that, compared with results in ideal situation, reconstructed images of all methods were influenced by noise to a certain extent. By analyzing image quality, we found that P-FDK had similar noise interference with direct FDK algorithm in case 1 and case 3. While in case 2, P-FDK method showed obviously higher resistance against noise compared with FDK. Both SART methods were also influenced by noise interference, but we can see that SART with TV regularization had higher resistance against noise, while the one with the absence of TV was seriously disturbed. SSIM dropped 2.2% for P-SART-TV after noise was added, while the same index dropped 7.7%, 11.7% and 32.2% in P-SART, P-FDK and FDK, respectively.

Meanwhile, although image quality and evaluation index had offered some support on evaluating algorithm performance. Detail information could be told by analyzing gray value on reconstructed results. As shown in Fig. 12, gray value of the 337$^{th}$ row under noise interference was plotted. The grayscale range of images was enlarged from [0,0.035] into [0,255]. It could be seen that in case 1 and case 3, P-FDK and P-SART had right structural information, while reconstructed images of FDK were not consistent with standard images. Besides, P-SART had a wider range of fluctuations compared with P-SART-TV. In case 2, all methods had right geometry structure. FDK and P-SART had more dramatic fluctuations compared with P-SART-TV method. P-FDK showed obviously lower gray value than ideal images in case 3. P-SART-TV showed the best consistent with standard images in all cases.

### B. EXPERIMENT RESULTS

A turkey leg was scanned in experiment. 200 slices were reconstructed using these methods with the slice thickness of 0.5 *mm*. The size of projection images we used in

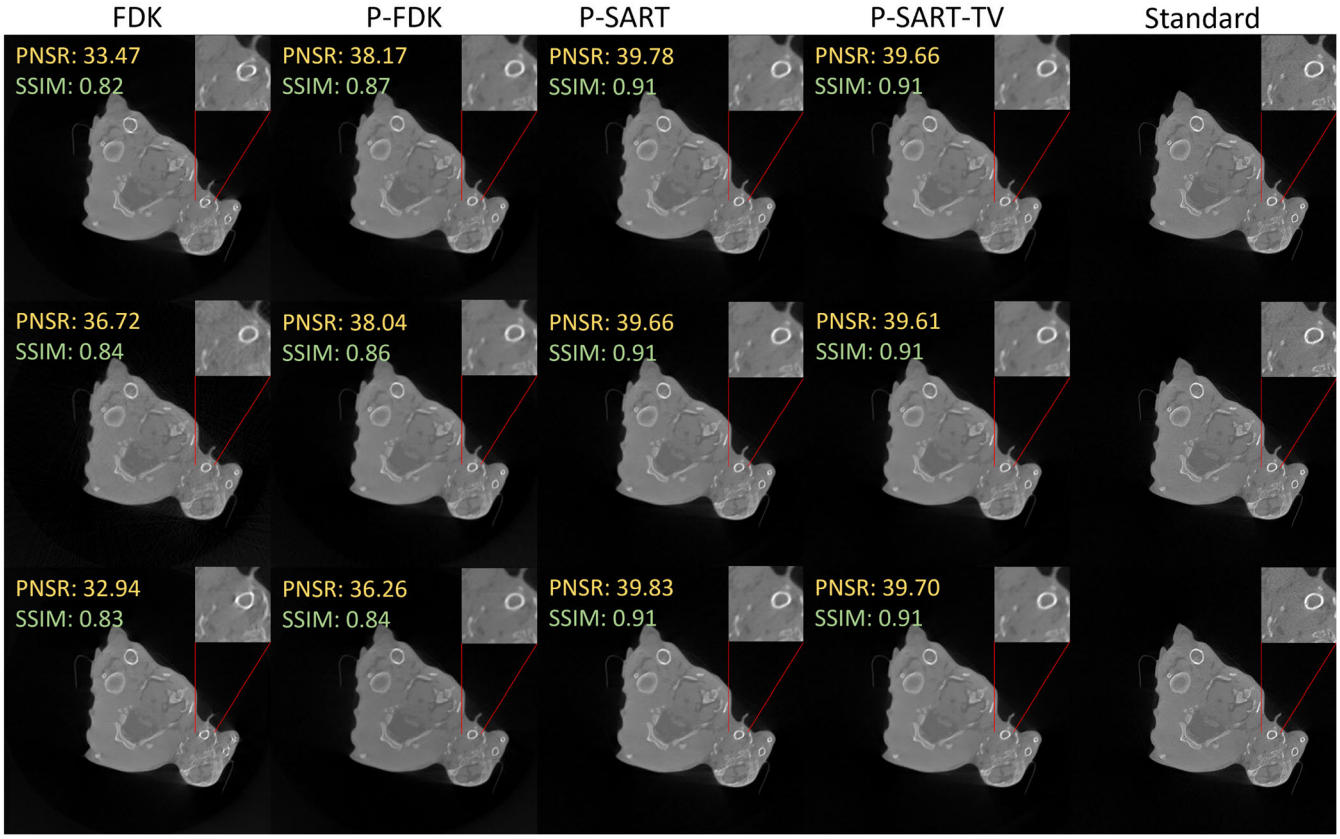


**FIGURE 10.** Simulation results without noise. (The reconstruction results of Case 1-3 were shown from top to bottom. From left to right were images using FDK, projection matrix-based FDK, projection matrix-based SART without TV, and projection matrix-based SART without TV, and projection matrix-based SART with TV).

reconstructions was 536 × 536 pixels, with pixel size of 0.8 *mm*. Reconstruction image size was 536×536 pixels, with pixel size of 0.35 *mm*. 110 projections within 220 degrees were used in reconstruction. Three slices were shown in Fig. 13, with gray scale range of [0,0.04]. We could see that mechanical errors of manipulators during scan would bring in mistakes, FDK without calibration would result in geometry artifacts in reconstructed images. Analyzing bone edges in the $140^{th}$ slice, we could see that these projection matrix-based methods were able to restore artifacts brough by motion error. And they achieved similar performance. However, when looking at the soft tissue in the $100^{th}$ slice, we could find that there was stripe artifact in reconstruction images of P-FDK, and P-SART-TV removed this artifact obviously. Besides, P-SART-TV provided the smoothest grayscale change in all three slices, and it had less noise interference compared with P-SART, which showed a better performance in real data.

It was worth mentioning that center of reconstructed image by FDK algorithm was inconsistent with other methods. This could be explained by different reconstruction centers of FDK algorithm and the projection matrix-based methods. Reconstruction center of FDK algorithm was the origin of world coordinate system, and reconstruction center of the latter was the origin of the phantom coordinate system. During data acquisition, it was hard to stay the center of calibration phantom at center of world coordinate system, which caused difference in reconstruction center.

## V. DISCUSSION AND CONCLUSION

Motion error often appeared during movement of manipulators, a calibration through projection matrix could bring correct geometry relationship into reconstructions. But P-FDK relied on circular scanning trajectory and introduced abnormal gray value under non-circular scanning trajectory. The back-projection weights of iterative method were determined through iterative solution and correct geometry definition could be provided by projection matrix. Therefore, we combined SART with projection matrix. Besides, real data were usually disturbed by noise. Regularization terms could be added into reconstruction to constrain interference in images.

Under ideal situation without noise, P-FDK showed good image quality in case 1 and case 2, which was barely the same with iterative methods. While its reconstructed image showed obvious abnormal gray value without artifacts in case 3. Meanwhile, P-SART showed the best image restoration performance in all cases. When noise was added into simulations, P-SART with regularization showed better resistance to noise. And in experiments, P-FDK and iterative methods achieved similar performance in image restoration, which is obviously better than traditional FDK.

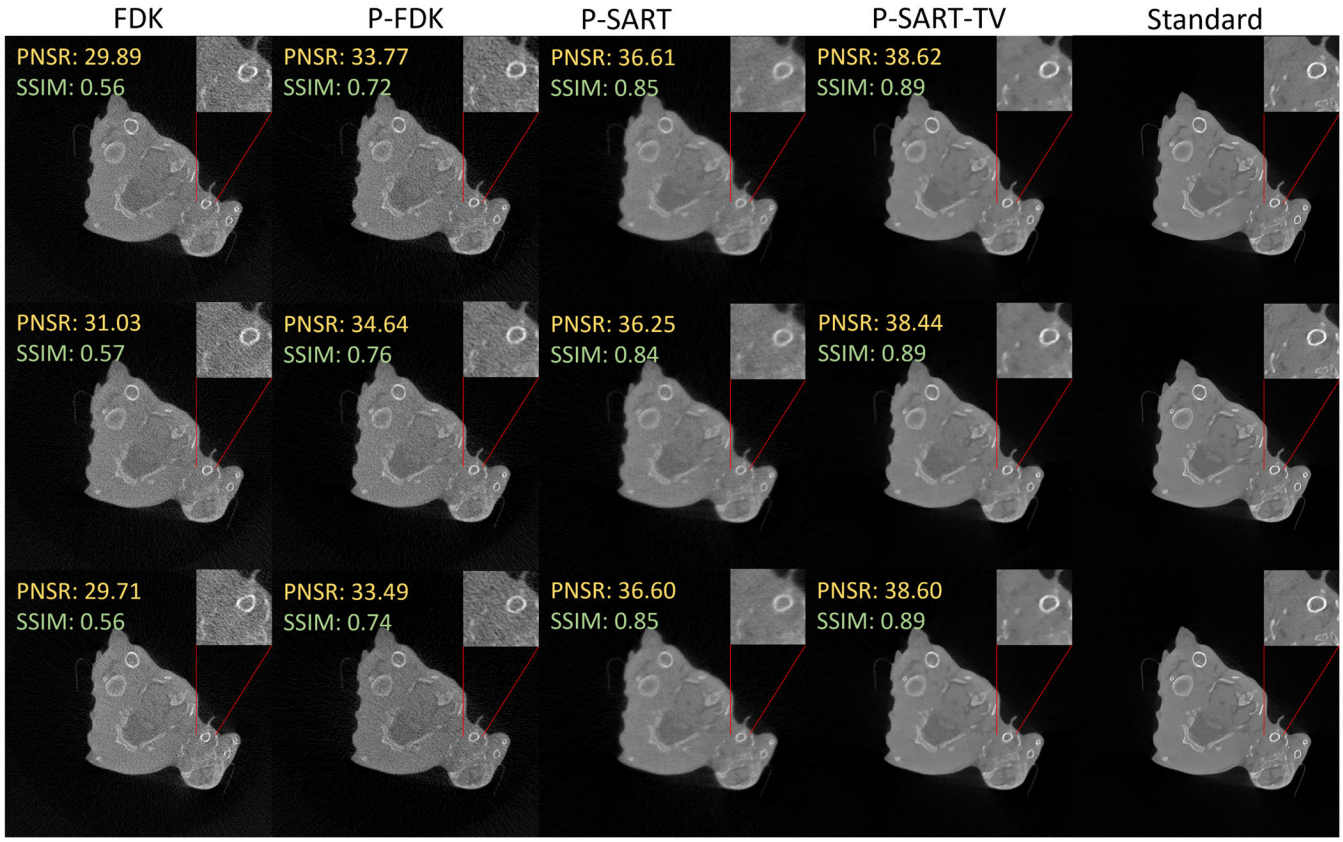


**FIGURE 11.** Simulation results with Poisson noise. (The reconstruction results of Case 1-3 were shown from top to bottom. From left to right were images using FDK, projection matrix-based FDK, projection matrix-based SART without TV, and projection matrix-based SART with TV).

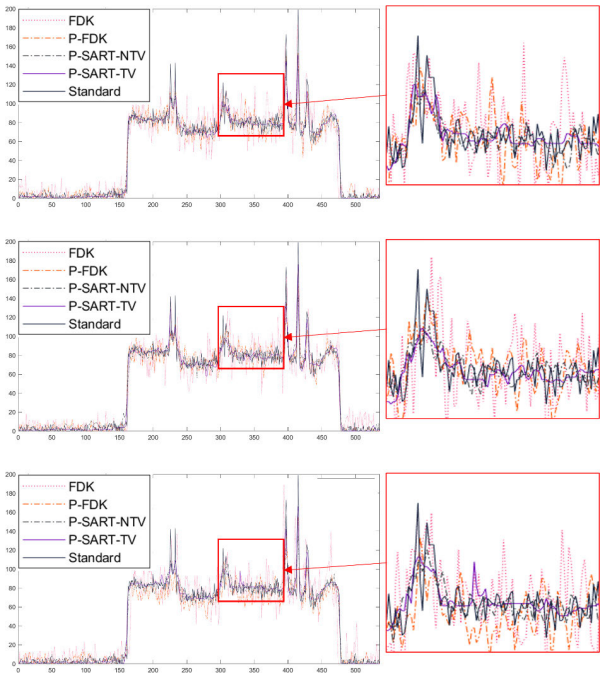


**FIGURE 12.** Image gray value evaluation. The reconstruction results of Case 1-3 are shown from top to bottom.

Considering that P-FDK and P-SART used the same projection matrix in expressing geometry relationship, both methods should be able to reconstruct images under motion error. Back-projection process of P-FDK method was depended on magnification ratio to determine weight value. In case 1 and case 2 of simulation, the motion error did not bring in obvious change in magnification ratio. This explained similar performance of P-FDK and P-SART. In case 3, however, magnification ratio under ellipse trajectory was obviously different from the one under circular trajectory. According to the way it deviated from real value, back-projection weight value became bigger or smaller than real value, which eventually caused abnormal gray value in images. Looking back at projection matrix-based iterative methods, image gray value was determined through iteration process. Calibrated geometry was converted into the algorithm through projection matrix. Because projection matrix was able to express geometry relationship under any scanning trajectory, Projection matrix-based iterative methods had better performance than others in all cases. When noise was added, P-SART-TV had obviously better resistance against noise interference because total variation was integrated into reconstruction process. In experiments, P-FDK had similar image quality with P-SART. This could be explained by approximate circular scanning trajectory of robotic CT.

The concept of a projection matrix was the foundation of the entire algorithm. A geometry calibration with phantom had to be performed before image reconstruction. As a

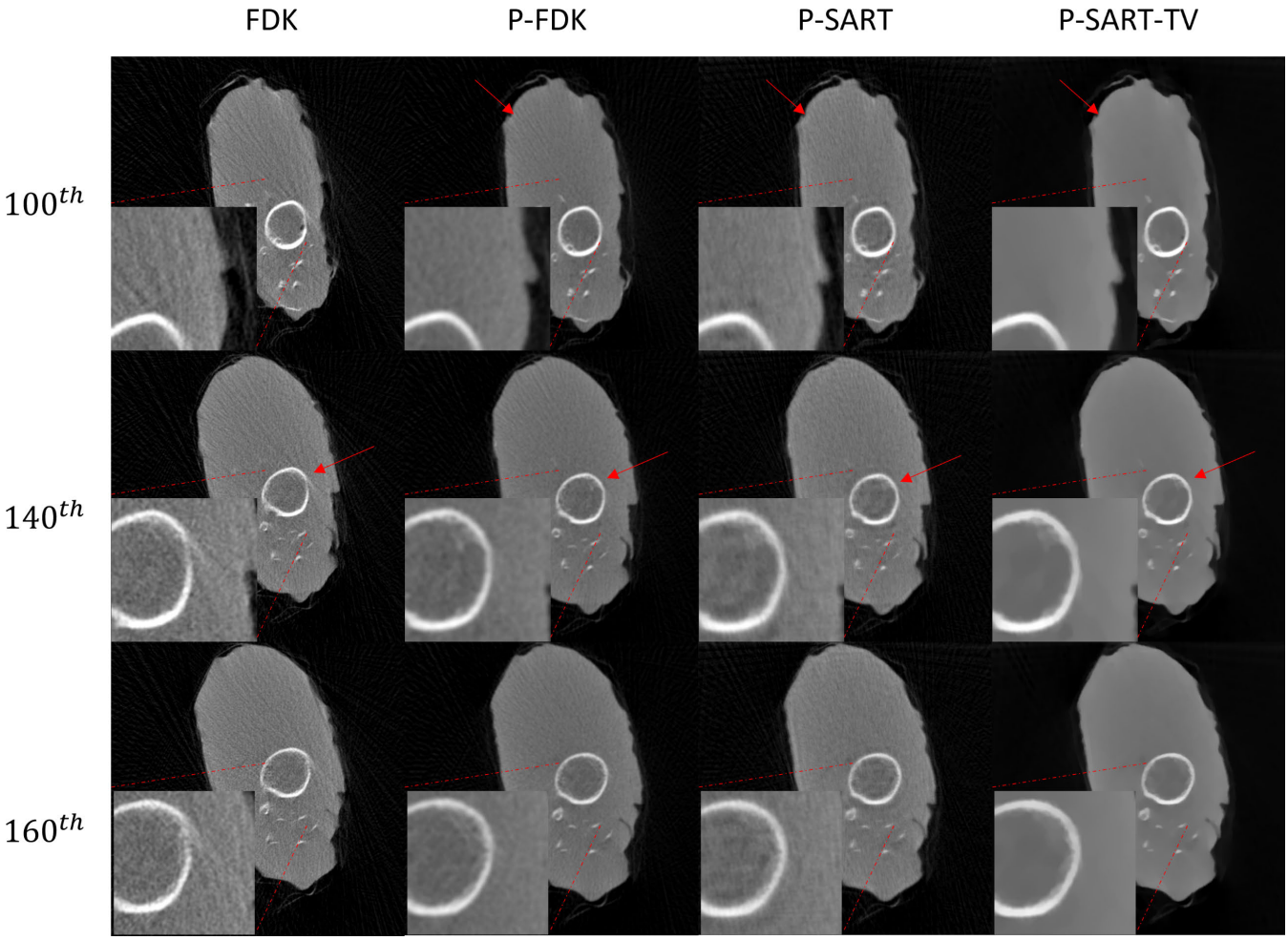


**FIGURE 13.** Reconstruction images in experiments (from left to right were images using FDK, projection matrix-based FDK, projection matrix-based SART without TV, and projection matrix-based SART with TV).

result, mistakes may be created during this procedure, including mistakes in center identification of projected image and error of phantom manufacturing. These mistakes would be further brought into projection matrix, which may bring in wrong geometry relationship into reconstruction eventually. Typical geometry calibration based on projection matrix involved matrix decomposition in order to gain geometry parameters. This process may introduce new error into final results because of non-uniform unit between different geometry parameters. FDK based on projection matrix skipped matrix decomposition and used projection matrix directly in reconstruction, which avoided mentioned error to a certain extent. But P-FDK was based on traditional FDK algorithm, which relied on circular scanning trajectory. P-FDK could not achieve good performance under arbitrary trajectory which was common in robotic CT, and might introduce wrong back-projection weights during reconstruction. The proposed iterative method combined projection matrix with iterative reconstruction. The geometry information of single angle was provided by projection matrix directly, back-projection value was determined by iteration process, which got rid of dependence on scanning trajectory. Besides, an experiment under arbitrary scanning trajectory could be conducted to further confirm the effectiveness of mentioned method.

In general, we proposed a new reconstruction algorithm, which was able to restore images under motion error of robotic CT, and verified its viability through simulation and experiments.

## REFERENCES

[1] G. T. Gullberg, B. M. W. Tsui, C. R. Crawford, and E. R. Edgerton, "Estimation of geometrical parameters for fan beam tomography," *Phys. Med. Biol.*, vol. 32, no. 12, pp. 1581–1594, Dec. 1987, doi: 10.1088/0031-9155/32/12/005.

[2] G. T. Gullberg, B. M. W. Tsui, C. R. Crawford, J. G. Ballard, and J. T. Hagius, "Estimation of geometrical parameters and collimator evaluation for cone beam tomography," *Med. Phys.*, vol. 17, no. 2, pp. 264–272, Mar. 1990, doi: 10.1118/1.596505.

[3] L. Li, Z. Chen, L. Zhang, Y. Xing, and K. Kang, "A cone-beam tomography system with a reduced size planar detector: A backprojection-filtration reconstruction algorithm as well as numerical and practical experiments," *Appl. Radiat. Isot.*, vol. 65, no. 9, pp. 1041–1047, Sep. 2007, doi: 10.1016/j.apradiso.2007.01.023.

[4] G. Li, S. Luo, C. You, M. Getzin, L. Zheng, G. Wang, and N. Gu, "A novel calibration method incorporating nonlinear optimization and ball-bearing markers for cone-beam CT with a parameterized trajectory," *Med. Phys.*, vol. 46, no. 1, pp. 152–164, Dec. 2018, doi: 10.1002/mp.13278.

[5] Y. Sun, Y. Hou, F. Zhao, and J. Hu, "A calibration method for misaligned scanner geometry in cone-beam computed tomography," *NDT E Int.*, vol. 39, no. 6, pp. 499–513, Sep. 2006, doi: 10.1016/j.ndteint.2006.03.002.
[6] K. M. Hanson, M. D. Silver, A. Sen, and S. Oishi, "Determination and correction of the wobble of a C-arm gantry," presented at the Med. Imag. Image Process., 2000.
[7] C. Mennessier and R. Clackdoyle, "Automated geometric calibration and reconstruction in circular cone-beam tomography," in *Proc. IEEE Nuclear Sci. Symp. Conf. Rec.*, Oct. 2008, pp. 5081–5085, doi: 10.1109/nssmic.2008.4774380.
[8] K. Yang, A. L. C. Kwan, D. F. Miller, and J. M. Boone, "A geometric calibration method for cone beam CT systems," *Med. Phys.*, vol. 33, no. 6, pp. 1695–1706, May 2006, doi: 10.1118/1.2198187.
[9] Y. Cho, D. J. Moseley, J. H. Siewerdsen, and D. A. Jaffray, "Accurate technique for complete geometric calibration of cone-beam computed tomography systems," *Med. Phys.*, vol. 32, no. 4, pp. 968–983, Mar. 2005, doi: 10.1118/1.1869652.
[10] N. K. Strobel, B. Heigl, T. M. Brunner, O. Schuetz, M. M. Mitschke, K. Wiesent, and T. Mertelmeier, "Improving 3D image quality of X-ray C-arm imaging systems by using properly designed pose determination systems for calibrating the projection geometry," in *Proc. SPIE*, Jun. 2003, pp. 943–954, doi: 10.1117/12.479945.
[11] J. Muders and J. Hesser, "Stable and robust geometric self-calibration for cone-beam CT using mutual information," *IEEE Trans. Nucl. Sci.*, vol. 61, no. 1, pp. 202–217, Feb. 2014, doi: 10.1109/TNS.2013.2293969.
[12] M. Xu, C. Zhang, X. Liu, and D. Li, "Direct determination of cone-beam geometric parameters using the helical phantom," *Phys. Medicin Biol.*, vol. 59, no. 19, p. 5667, 2014, doi: 10.1088/0031-9155/59/19/5667.
[13] X. Li, D. Zhang, and B. Liu, "A generic geometric calibration method for tomographic imaging systems with flat-panel detectors—A detailed implementation guide," *Med. Phys.*, vol. 37, no. 7, pp. 3844–3854, Jun. 2010, doi: 10.1118/1.3431996.
[14] M. Chen, Y. Xi, W. Cong, B. Liu, B. Wei, and G. Wang, "X-ray CT geometrical calibration via locally linear embedding," *J. X-Ray Sci. Technol.*, vol. 24, no. 2, pp. 241–256, Mar. 2016, doi: 10.3233/XST-160548.
[15] M. Chen, P. He, P. Feng, B. Liu, Q. Yang, B. Wei, and G. Wang, "General rigid motion correction for computed tomography imaging based on locally linear embedding," *Opt. Eng.*, vol. 57, no. 2, 2018, Art. no. 023102, doi: 10.1117/1.OE.57.2.023102.
[16] M. Li, C. Lowe, A. Butler, P. Butler, and G. Wang, "Motion correction via locally linear embedding for helical photon-counting CT," in *Proc. SPIE*, 2022, pp. 559–567.
[17] M. Li, J. Bohacova, J. Uher, W. Cong, J. Rubinstein, and G. Wang, "Motion correction for robot-based X-ray photon-counting CT at ultrahigh resolution," in *Proc. SPIE*, 2022, pp. 172–181.
[18] Y. Xu, S. Yang, J. Ma, B. Li, S. Wu, H. Qi, and L. Zhou, "Simultaneous calibration phantom commission and geometry calibration in cone beam CT," *Phys. Med. Biol.*, vol. 62, no. 17, pp. N375–N390, Aug. 2017, doi: 10.1088/1361-6560/aa77e5.
[19] X. Duan, J. Cai, Q. Ling, Y. Huang, H. Qi, Y. Chen, L. Zhou, and Y. Xu, "Knowledge-based self-calibration method of calibration phantom by and for accurate robot-based CT imaging systems," *Knowl.-Based Syst.*, vol. 229, Oct. 2021, Art. no. 107343, doi: 10.1016/j.knosys.2021.107343.
[20] K. Wiesent, K. Barth, N. Navab, P. Durlak, T. Brunner, O. Schuetz, and W. Seissler, "Enhanced 3-D-reconstruction algorithm for C-arm systems suitable for interventional procedures," *IEEE Trans. Med. Imag.*, vol. 19, no. 5, pp. 391–403, May 2000, doi: 10.1109/42.870250.
[21] D. Kazantsev, V. Pickalov, S. Nagella, E. Pasca, and P. J. Withers, "Tomo-Phantom, a software package to generate 2D–4D analytical phantoms for CT image reconstruction algorithm benchmarks," *SoftwareX*, vol. 7, pp. 150–155, Jan. 2018, doi: 10.1016/j.softx.2018.05.003.
[22] W. van Aarle, W. J. Palenstijn, J. De Beenhouwer, T. Altantzis, S. Bals, K. J. Batenburg, and J. Sijbers, "The ASTRA toolbox: A platform for advanced algorithm development in electron tomography," *Ultramicroscopy*, vol. 157, pp. 35–47, Oct. 2015, doi: 10.1016/j.ultramic.2015.05.002.

**XUAN ZHOU** received the B.S. degree in medical imaging technique from Sichuan University, Sichuan, China, in 2020. He is currently pursuing the Ph.D. degree in particle physics and nuclear physics with the Chinese Academy of Science, Beijing, China. His research interests include geometry calibration method and reconstruction algorithm in robotic CT.

**QIONG XU** received the B.S. and Ph.D. degrees in information and communication engineering from Xi'an Jiaotong University, Xi'an, China, in 2005 and 2012, respectively. She is currently an Associate Professor with the Institution of High Energy Physics, Chinese Academy of Science. Her research interests include CT reconstruction algorithm and system development.

**CUNFENG WEI** received the B.S. and Ph.D. degrees in nuclear science and techniques from Lanzhou University, Lanzhou, China, in 2001 and 2006, respectively. He is currently a Professor with the Institution of High Energy Physics, Chinese Academy of Science. His research interests include X-ray imaging and reconstruction algorithm.